Catalytic consequences of ultrafine Pt clusters supported on SrTiO3 for photocatalytic overall water splitting

Muhammad Iqbal Qureshi, Angel T Garcia-Esparza, Gabriel Jeantelot, Samy Ould-Chikh, Antonio Aguilar-Tapia, Jean-Louis Hazemann, Jean-Marie Basset, David Loffreda, Tangui Le Bahers, Kazuhiro Takanabe

Catalytic consequences of ultrafine Pt clusters supported on $SrTiO_3$ for photocatalytic overall water splitting

Muhammad Qureshi [a], Angel T. Garcia-Esparza [b,1], Gabriel Jeantelot [a], Samy Ould-Chikh [a], Antonio Aguilar-Tapia [c], Jean-Louis Hazemann [c], Jean-Marie Basset [a], David Loffreda [b], Tangui Le Bahers [b], Kazuhiro Takanabe [a,d,⇑]

[a] King Abdullah University of Science and Technology (KAUST), KAUST Catalysis Center (KCC) and Physical Sciences and Engineering Division, 4700 KAUST, Thuwal 23955-6900, Saudi Arabia
[b] Univ Lyon, ENS de Lyon, CNRS, Université Claude Bernard Lyon 1, Laboratoire de Chimie UMR 5182, F-69342 Lyon, France
[c] Institut Néel, UPR 2940 CNRS–Université Grenoble Alpes, F-38000 Grenoble, France
[d] Department of Chemical System Engineering, School of Engineering, The University of Tokyo, 7-3-1 Hongo, Bunkyo-ku, Tokyo 113-8656, Japan

Keywords:
Photocatalysis
Density functional theory
Platinum
Particle size effect
Water splitting
CO poisoning
Strontium titanate
Hydrogen evolution

a b s t r a c t

The metal cluster size in supported metal catalysts impacts the oxidation state of the metal atoms, coordination capability, and finally the catalytic activity—especially when the number of atoms becomes countable. The correlation between metal oxidation state and its catalytic consequences for ultrafine Pt was studied for photocatalytic overall water splitting using a $Pt/SrTiO_3$ (photo)catalyst. A distinctive change in catalytic behavior and oxidation state was observed below 100 Pt-atom clusters at ~2 nm. Combining density functional theory (DFT) and experimental characterizations including X-ray absorption spectroscopy (XAS), X-ray photoelectron spectroscopy (XPS), and diffuse reflectance infrared Fourier transform spectroscopy (DRIFTS), the smaller Pt clusters obtained by the surface organometallic route (under 100 Pt atoms) were predominantly oxidized and selectively performed photocatalytic water splitting selectively without activation of the water-forming back-reaction from H_2 and O_2. When the Pt clusters obtained by classical impregnation were larger than 2 nm, they remained metallic (Pt^0) and were active for both water splitting and the competing thermal water formation back reaction. In addition, Pt^0 clusters are poisoned in the presence of CO, whereas highly dispersed ultra-fine oxidized Pt clusters are insensitive to CO. This paper presents evidence of ultrafine PtO_x (below approximately 2 nm clusters) that are insensitive to coordination of various gas identities (H_2, O_2, CO), resulting in efficient and selective photocatalytic overall water splitting.

1. Introduction

The cluster size of active metals in supported metal catalysts often leads to critical catalytic consequences [1]. The size effects are understood based on electronic effects and geometric effects, which are inter-correlated and strongly affected by the presence of a support [1,2]. The electronic structures of metal clusters are influenced by the interaction with the support, and such influence increases as the metal cluster size decreases. A quantitative description of such interactions at the atomic scale of the cluster is generally challenging both experimentally and computationally. Recent advances in density functional theory (DFT) calculations allow determination and interpretation of the charge reorganization induced by the interaction and of the charge transfer between the metal and the support [3,4]. Therefore, this theory opens a pathway to the atomistic interpretation of the experimentally measured properties of these systems. In addition, a variation in the cluster size simultaneously causes changes in the exposed geometric surface morphology of the metal (facet): more low-coordination sites are exposed as the cluster size decreases [5]. The reactivity on different facets may cause drastic differences in catalytic reactivity for various reactions [6,7]. The reactions affected by the cluster size are called structure-sensitive reactions [6]. This geometric effect is inevitably linked to electronic effects—especially when the support interacts strongly with the cluster [8].

⇑ Corresponding author at: Department of Chemical System Engineering, School of Engineering, The University of Tokyo, 7-3-1 Hongo, Bunkyo-ku, Tokyo 113-8656, Japan.
E-mail address: takanabe@chemsys.t.u-tokyo.ac.jp (K. Takanabe).
[1] Present address: Stanford Synchrotron Radiation Light Source, SLAC National Accelerator Laboratory, Menlo Park, CA 94025, USA.

One way to quantify the electronic interaction between oxide supports and metal nanoparticles is simulation of the density of states of a model catalyst. Lykhach et al. [9] and Kozlov et al. [10] reported a good example that quantified the degree of electronic metal-support interaction (EMSI) when Pt nanoparticles are supported on CeO_2. The DFT calculations (GGA + U) nicely coincide with the potential shift in Pt nanoparticles as measured by X-ray photoelectron spectroscopy (XPS). The extent of electron exchange at steady state under vacuum is maximized when the particle size is 1–8 nm or 100– atoms.

Another important aspect is the geometric effects arising from the size of the metal nanoparticles. For example, the size of Pt nanoparticles has a strong impact on the electrocatalytic oxygen reduction reaction (ORR)—this is one of the most investigated electrocatalytic reactions with practical value to fuel cell technology [11]. The ORR is a structure-sensitive reaction with distinctive catalytic activity for Pt(1 1 1), Pt(1 0 0), and Pt(1 1 0) [11]. Several research groups have observed that Pt nanoparticles lose specific activity and mass activity when the particles become smaller than 2nm [12–16]. Recently, a combined experimental and theoretical approach of ORR at various Pt nanoparticle size and extended surfaces has shown that the electrocatalytic activity toward ORR can be captured by the generalized coordination number of active sites (where the surface species such as $^*OH$ and $^*OOH$ are bound) [16]. Besides, the loss of performance between Pt(1 1 1) and Pt nanoparticles of ~2 nm can be explained by a loss of coordination for $^*OH$ intermediate at the active site [16]. One explanation for the loss of the activity below ~2 nm is strong coordination of adsorbed oxygen as a consequence of the size and the shape of the nanoparticles [11]. Another possible explanation that has been experimentally proven is that these small Pt clusters are oxidized and cannot maintain a metallic state [17]. As expected, oxidized Pt particles rarely have high catalytic activity in oxidation reactions [17–20].

Recently, single-atom supported catalysis has been shown with activity and selectivity that are unique to the various catalytic reactions [21–24]. Yang et al. observed a single-site in its oxidized form, namely Pt(II)-$O(OH)_x$. This can be further influenced by other elements such as Na [25]. This single-site Pt catalyst is active for CO oxidation and water gas shift reactions with some controversy in the active sites as argued by Ding et al. who claimed that the Pt single sites act more as spectators because the binding energy to CO is high [26]. It is always challenging, however, to maintain high dispersion of metal sites, as they are susceptible to sintering especially under the reaction conditions (heat, adsorption, light, etc.).

Decoration of semiconductor photon-absorbers with metal catalysts, e.g., Pt nanoparticles, is essential to achieve efficient overall water splitting (OWS); however, these metal nanoparticles can also catalyze the water-forming back reaction from H_2 and O_2 products, thereby decreasing the overall efficiency of the system [27]. A general strategy to suppress the back reaction is to apply semipermeable membrane coatings on the metal surfaces such as CrO_x [27–29], NiO_x [30–32], MoO_x [33], SiO_x [34,35], and Ti, Nb, and Ta oxyhydroxides [36,37]. Nevertheless, a rigorous study on the particle size dependence is still lacking in the literature for the OWS. A relevant example was demonstrated by Li et al. where the Pt in Pt/TiO_2 photocatalyst remained oxidized when the Pt particle was as small as ~1 nm [38]. In their report, they discuss that oxidized Pt cannot react with H_2 and O_2 under dark conditions. This offered a monotonic accumulation of H_2 that evolved from 30 vol% methanol aqueous solution in the presence of O_2. This concept could certainly be applied for photocatalytic OWS where H_2 and O_2 are simultaneously cogenerated.

Here, we describe our efforts to understand the Pt size effects that describe the Pt/$SrTiO_3$ system for photocatalytic OWS. We performed DFT calculations on several sizes of Pt clusters adsorbed on a $SrTiO_3$ surface to understand the size-effect on the EMSI as well as the ability of the Pt nanoclusters to be oxidized. These calculations were based on the work functions, Bader charge analysis, and mapping of the charge density differences between the clusters and the oxide support. Distinctive photocatalytic behaviors were observed experimentally by controlling the cluster-size of the Pt on $SrTiO_3$. The ultrafine Pt nanoclusters were less than ~2 nm and were synthesized on the $SrTiO_3$ surface via a surface organometallic chemistry (SOMC) grafting approach. These small Pt clusters showed stable OWS performance with no signs of a water-formation back reaction even under dark conditions. A size of approximately 2 nm was identified as the threshold, and decoration with larger Pt clusters—either synthesized by sintering the SOMC sample or the impregnation method—lead to a competitive loss of the OWS performance with a thermal back reaction that occurs regardless of illumination. X-ray photoelectron spectroscopy (XPS), X-ray absorption spectroscopy (XAS), and diffuse reflectance infrared Fourier transformed spectroscopy (DRIFTS) were used to characterize the nature of Pt. All of the characterizations demonstrated that the small Pt clusters were found to be in an oxidized state (Pt^{2+}) becoming selective to OWS. The larger clusters, which cause the back reaction, were metallic (Pt^0). Such metallic sites are effectively poisoned by CO gas, while oxidized sites are essentially insensitive to the presence of CO.

2. Experimental and theoretical

2.1. Synthesis

The synthesis of $SrTiO_3$ was based on the literature [39] where $SrTiO_3$ powder and $SrCl_2$ at a molar ratio of 1:5 were prepared with a mortar and pestle for 25 min followed by a flux treatment at 1273 K for 10 h in an alumina crucible to generate highly crystalline $SrTiO_3$. The powder was collected and washed continuously with water (approximately 1 L) until no chloride salt was detected via a $AgNO_3$ test.

The grafting of (1,5-cyclooctadiene) dimethylplatinum(II) [(COD)Pt(CH_3)$_2$] on $SrTiO_3$ was done using standard surface organometallic chemistry (SOMC) techniques (grafting setup schematic available in Fig. S1). One gram of flux-treated $SrTiO_3$ was placed in the second half of a double-Schlenk. To remove any physisorbed water, a dehydroxylation treatment was performed where the Schlenk line was connected to a high vacuum; a dynamic vacuum of $1x10^{-5}$ mbar was applied with a heat treatment at 200 °C overnight. The Schlenk line was then opened in a glovebox under an inert atmosphere (Ar), and 8.5 mg of (COD)Pt(CH_3)$_2$ was introduced in the first half of the double Schlenk. Vacuum was again pulled on the double-Schlenk and its contents. Dry and oxygen-free pentane were vacuum-transferred to the first half of the Schlenk (15 mL), and left to stir until full dissolution of the platinum complex. The solution was then filtered across the frit into the second half of the double-Schlenk for grafting on the $SrTiO_3$ powder to proceed.

The resulting suspension was stirred, sonicated in an ultrasonic bath, and left to stir overnight. The pentane solution containing excess platinum precursor was filtered back into the first half of the double-Schlenk. Washings were then performed via vacuum-transferring pentane on the $SrTiO_3$, stirring the suspension, and filtering it back through the frit into the first half of the double-Schlenk. This cycle was repeated five times. Solvent in the double-Schlenk was then vacuum-transferred to an empty flask, and a dynamic vacuum (1×10^{-5} mbar) was pulled on the sample overnight to thoroughly dry it. The double-Schlenk was then opened in a glovebox under inert atmosphere where the grafted $SrTiO_3$ was transferred into a storage tube for further use. The sample is denoted as Pt/$SrTiO_3$ (GT). Another sample was obtained by

the heat treatment of this sample at 300 °C in static air using a muffle furnace. This sample is denoted as Pt/$SrTiO_3$ (GT-300).

For the impregnation method, 0.1 M Na_2PtCl_6-$6H_2O$ aq. solution was mixed with 100 mg of $SrTiO_3$ over a water-bath in 5 mL of water until all the water evaporated. The powder was collected by filtration and calcined at 300 °C for 1 h.

2.2. Photocatalytic test

The photocatalytic reactions were conducted with 100 mL of an ultra-pure water (18.2 MX cm) and 50 mg of photocatalyst at 100 Torr of Ar gas in a circulating batch reactor equipped with an online gas chromatograph (GC: Bruker 450 GC, TCD, Ar gas, molecular sieve 13X) connected to a vacuum line. For experiments with methanol aqueous solution, the solution consisted of 90 mL ultra-pure water and 10 mL methanol. For the CO gas experiments, 5% CO gas (Ar balance) was bubbled through the 100 mL of the ultra-pure water/catalyst mixture for 20 min, and the photocat- alytic reaction was performed at 100 Torr with 5% CO gas. A Xe lamp (CERMAX PE300-BF, 300 W) was used as the light source, and the irradiation wavelength was controlled via a combination of a cold mirror and a water filter (300 < k < 800 nm). The irradi- ance is shown in Fig. S2a. The spectral area of the photocatalytic reactor was 38.5 cm^2. For quantum efficiency calculations, the pho- ton flux was measured using the AvaSpec-3648 spectrometer, an AvaLight DHS calibration light source, and a FC-UV200-2 fiber-optic cable. The apparent quantum efficiency (AQE) measurement was conducted with a 350-nm bandpass filter. The irradiance is shown in Fig. S2b.

2.3. Characterization

DRIFTS measurements were acquired using a Thermo Scientific Nicolet 6700 FT-IR spectrometer with a mercury-cadmium telluride (MCT) detector and a Harrick Praying Mantis diffuse reflectance accessory. The optical velocity was set to 0.63, and the aperture was set to 64. The samples were placed in a Harrick High Temperature Reaction Chamber with ZnSe windows. The cell was first flushed with argon and then heated at 120 °C for 1 h to remove moisture followed by cooling back down to room temp before the introduction of 5% CO gas at a flow rate of 5 mL min^{-1}.

Electron microscopy of samples was performed by using a Titan ThemisZ transmission electron microscope (TEM) from Thermo-Fisher Scientific. The microscope was operated at an accelerating voltage of 300 kV using the scanning TEM (STEM) mode. The spherical aberration coefficient of the electron beam was corrected in the STEM using a CESCOR from CEOS, GmbH. The images were acquired over a range of magnifications, and the entire image-acquisition was performed in the Gatan Microscopy Suite of version GMS 2.5 from Gatan, Inc.

XPS spectra were obtained with an AMICUS KRATOS using an Al anode at 15 mA and 8 kV. A peak maximum of C 1 s at 284.8 eV was used as an internal standard to correct the binding energies. ICP measurements were performed using an ICP-OES Varian 72 ES, and the amounts of loaded catalysts are reported using the measured values.

The Pt L_3-edge HERFD-XANES spectra were recorded at the European Synchrotron Radiation Facility on the CRG-FAME-UHD beamline (BM16). The beamline was equipped with a liquid nitrogen-cooled double-crystal Si(2 2 0) monochromator surrounded by two Rh-coated mirrors for harmonic rejection. The beam size on the sample was held constant during an energy scan of around 220 × 110 lm (horizontal × vertical, FWHM). The [6 6 0] reflection of the three Ge(1 1 0) spherically bent crystal analyzers (bending radius of 1 m) from the multi-crystal spectrometer installed at BM16 were used to select the La1 (L_3-M_5) fluorescence line at 9442 eV. The total energy resolution of the HERFD-XANES data was estimated to be approximately 0.7 eV. Energy calibration of the incoming radiation was performed prior to the measurements by recording the L_3-edge transmission spectrum of a Pt foil and assigning the maximum of the first derivative peak to 11564 eV.

The XAS data were analyzed using the HORAE package—a graphical interface to the AUTOBK and IFEFFIT code [40]. The XANES and EXAFS spectra were obtained after performing standard procedures for pre-edge subtraction, normalization, polynomial removal, and wave vector conversion. The extracted EXAFS signals were Fourier transformed using a Kaiser-Bessel apodization window (dk = 1) within a k-range of about [3.5; 10–12] $Å^{-1}$ for all samples. Continuous Cauchy wavelet transform was also applied to simultaneously decompose the EXAFS signal in the reciprocal and real spaces [41].

2.4. Theoretical calculations

The density functional theory (DFT) calculations were performed in periodic boundary conditions with the Vienna *Ab initio* Simulation Package (VASP 5.4.1). The electron–ion interactions are described by the PAW formalism [42]. The DFT + U approach was used to describe the spin-polarized electronic structures at the generalized gradient approximation (GGA) level with the PBE functional along with a Hubbard correction (GGA-PBE + U) [43,44], with an energy cut-off of 400 eV for the plane-wave basis set, with a G-centered 1×1×1 k-point mesh, and $U_{eff,\ Ti}$ = 5.0 eV according to Dudarev's model. All the geometries were fully optimized to gradients smaller than 0.01 eV·$Å^{-1}$, the wave-functions converged to an SCF energy of 10^{-6} eV, and the electronic occupancies were determined by the Fermi smearing method using a smearing of 0.01 eV. Accounting for solvation effects was performed via the implicit solvation model as implemented by Mathew et al. (VASPsol) [45]. The dielectric constant of bulk water (ϵ = 80) was used with the default and previously reported technical settings [46,47]. In this implicit solvation model, the polarization of the system due to the solvent is included self-consistently [46]. This solvation model was already applied to similar systems (platinum clusters in contact with water) [48]. A density-dependent dispersion correction dDsC developed by Steinmann et al. has been applied in the calculations to account for weak non-bonded interactions [48]. The density of states was computed for the optimized geometries by Gaussian smearing with a smearing value of 0.1 eV.

3. Results

3.1. DFT analysis of the interaction between Pt clusters and $SrTiO_3$

We investigated the cluster size effect on the electronic structure at the interface of Pt and $SrTiO_3$(0 0 1) surface hydrated by an implicit water solvent. We performed GGA + U-dDsC calculations of different Pt clusters adsorbed on a TiO_2 terminated $SrTiO_3$(0 0 1) surface, after having considered a stable termination for the oxide [47,49,50]. The choice of the support termination (0 0 1) is motivated by the acceptable compromise between the relevance of the provided theoretical results with respect to measurements and the high computational cost to achieve DFT + U calculations for such large systems. Four sizes of Pt clusters were simulated containing 1 (Pt_1), 25 (Pt_{25}), 50 (Pt_{50}), and 119 (Pt_{119}) Pt atoms. Pt_{25}, Pt_{50} and Pt_{119} correspond to respective truncated octahedral clusters Pt_{38}, Pt_{79} and Pt_{201} (known to be competitive in terms of stability in the range 1–2 nm, see for instance ref. [16]), of which less than half the atomic layers have been removed

to maximize the number of chemical bonds between the Pt cluster and the oxide support (thus its stability), as depicted in Fig. 1a. This choice leads to an interface angle between the (1 1 1) and (1 0 0)-type facets and the oxide support, comprised in the range 90–180° (obtuse angle). Other morphology of particles can be stable for such small clusters, but we expect that due to the minimal lattice mismatch of 0.4% a cube-on-cube epitaxial growth dominates and the main shape and properties of the interaction between Pt (a_{Pt} = 3.920 Å) and $SrTiO_3$ (a_{STO} = 3.905 Å) will remain similar. The $SrTiO_3$(0 0 1) surface was modelled by a (6x6) supercell 5-layers slab (Fig. 1a). Convergence of the surface energy is given in the supporting information Fig. S3 to support the 5-layer slab thickness choice. The geometry of the four supported Pt nanoclusters has been relaxed completely, and the electronic analyses have been calculated on the optimal structures. The particle sizes correspond to the distance between the furthest nucleus of Pt atoms plus the atomic radius of Pt.

The Fermi level of the bare $SrTiO_3$ surface is more negatively located than that of unsupported Pt bulk (see Table S1). Thus, from the systems' bare components point-of-view—and due to the work function differences—an electron transfer from $SrTiO_3$ to Pt particles is thermodynamically expected once Pt clusters are adsorbed on the surface in order to equalize the Fermi energies. The defects in the $SrTiO_3$ would increase the Fermi level promoting the semiconductor to inject electrons into Pt on the surface, and thus we would expect a relatively larger charge transfer overall but conserving the calculated DFT trend. Indeed, based on Bader analysis, a charge transfer from the $SrTiO_3$ to Pt was computed and the results are demonstrated in Fig. 2. A larger Pt cluster implies a larger charge transfer. The amount of transferred charge appears to saturate as the particle size increases. Such phenomenon has been experimentally characterized for Pt nanoparticles adsorbed on ceria [9]. The fraction of transferred charge converges to zero when divided by the number of Pt atoms in the cluster (Fig. 2). In other words, fewer Pt atoms in the cluster are affected by the charge transfer as the Pt cluster size increases and vice versa.

$$Dq = q(Pt_n/SrTiO_3) - q(Pt_n) - q(SrTiO_3) \quad (1)$$

Interestingly, when calculating the difference in charge density between Pt and $SrTiO_3$ and drawing the electron density reorganization map (Eq. (1), Fig. 1b), we observed that only the Pt atoms from the first two layers in contact with $SrTiO_3$ are significantly affected by the charge transfer when the size reaches ~2 nm. These results are compatible with a previous DFT + U study of Pt_{95} and P_{122} nanoclusters supported on stoichiometric CeO_2(1 1 1) showing that the charge transfer only affects the interfacial Pt atoms between the metallic nanoparticle and the oxide support, although the overall transfer is opposite to the one obtained in the work [10]. On the other hand, the Fermi energy of the $Pt_n/SrTiO_3$ system decreases as the Pt cluster size increases, and the calculated values are between those of the two bare materials (Fig. 1c, Table S1). The Fermi energy corresponds to the work function of the material, and thus is directly correlated to the ability to remove electrons from the system (i.e. oxidation potential). Consequently, a lower Fermi level energy implies increased difficulty in oxidizing the system. Overall, the computations show a 0.5 eV difference in the Fermi energy between the supported Pt_{25}, Pt_{50}, and Pt_{119} systems. The work function of small clusters and single-atoms on $SrTiO_3$ are

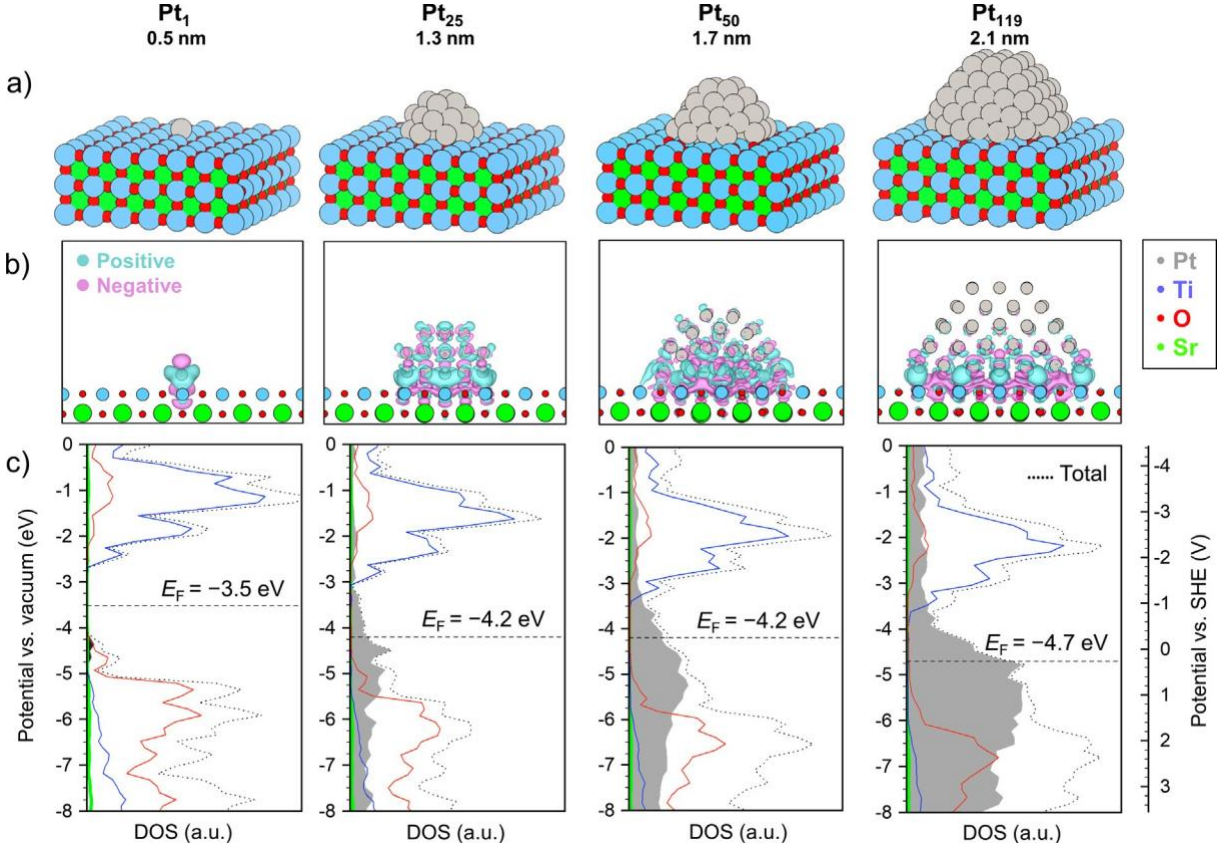

Fig. 1. (a) The DFT optimized structures of Pt_1, Pt_{25}, Pt_{50}, and Pt_{119} clusters adsorbed on the $SrTiO_3$(0 0 1) surface along with the size of the Pt cluster (larger Pt-Pt distance increased the Pt atomic radius). (b) The charge density difference isosurface maps (isosurface level is 0.003 e^- $Bohr^{-3}$) and (c) the density of states computed for the four systems at the GGA + U-dDsC level. The Fermi level is shown with reference to the vacuum level.

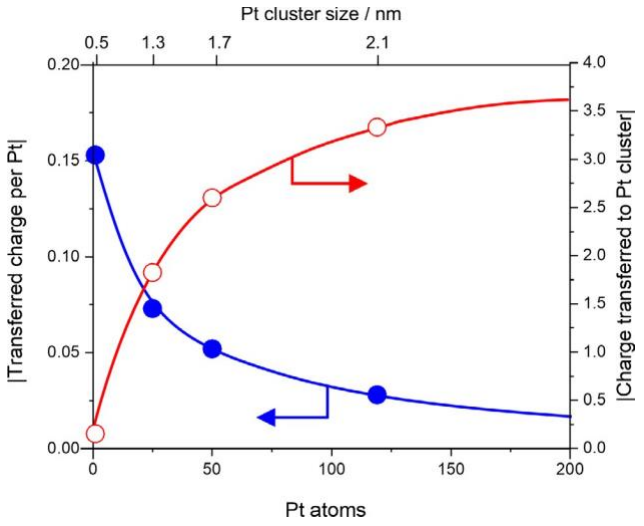

Fig. 2. Total charge transfer from $SrTiO_3$ to Pt clusters (open symbol in red) and per Pt atoms (closed symbol in blue) reported as a fraction of the fundamental charge as a function of cluster size.

closer to the semiconductor's electron affinity and more negative than 0 V in the standard hydrogen electrode scale (Fig. 1c, Table S1) as previously noted.

On the contrary, the Pt_{119} work function increases towards a similar range as the isolated Pt nanoparticles (more negative than −5.0 eV, Table S1) and clean Pt surfaces. Previously reported values range between -5.0 to -5.9 eV depending on the exposed facet—this is consistent with our calculated values in Table S1 [51]. As a consequence, the smaller clusters have more electrons and will be more easily oxidized; the larger nanoparticles will behave similarly to difficult-to-oxidize bulk platinum (the reported work function range of Pt is -5.6 to -6.0 eV) [52]. From these calculations, we can expect that the Pt clusters smaller than 100 atoms adsorbed on $SrTiO_3$ can be oxidized compared to larger Pt nanoparticles (>~2 nm). Moreover, Pt atoms close to the $Pt/SrTiO_3$ interface are more susceptible to oxidation—we have observed that atoms directly in contact with $SrTiO_3$ surfaces are markedly influenced by electron transfer, and thus reflect a larger EMSI (Fig. 1b). We note here that small clusters are composed of mostly surface atoms that are accessible for oxidation (1 nm cluster corresponds to >60% of surface atoms); in larger clusters, the atoms prone to oxidation due to charge transfer are in the minority. Most are not surface atoms (larger bulk-to-surface atoms ratio), and thus they are far more stable toward oxidations from external oxidants in the environment. These theoretical results show an obviously different behavior towards oxidation and catalytic reactivity from Pt clusters adsorbed on $SrTiO_3$ as a function of cluster size.

According to the previous combined experimental and computational works presented in the literature in the case of Pt clusters adsorbed on *C*-alumina surface, it appears that the smaller the platinum cluster, the larger the reactivity toward its oxidation [53]. As a matter of fact, in the presence of oxygen/water, thermodynamically Pt_{13} cluster can be easily oxidized up to the $Pt_{13}O_{24}$ stoichiometry even at room temperature [54]. Furthermore, the oxidation of the Pt clusters was found to prevent from their sintering. It was also highlighted that adsorption of O_2 molecules on Pt clusters was favored at shared sites between the Pt atoms and the support surface's atoms. In all, it is consistent with our observation that the small cluster would be easily oxidized as a consequence of the larger number of interfacial sites for small cluster systems than for large cluster systems and synergistic catalytic effects at the interface between the Pt particles and the support.

3.2. Synthesis of different Pt size in $Pt/SrTiO_3$.

The $SrTiO_3$ photocatalyst was synthesized following the reported protocol to obtain a state-of-the-art semiconductor for high photocatalytic performance [39]. It is a challenge to synthesize highly-dispersed Pt supported on $SrTiO_3$ free from ionic impurities associated with metal precursors. The SOMC method was thus applied for surface hydroxyl species. Here, $SrTiO_3$ is used to graft $(COD)Pt(CH_3)_2$ precursors that form methane gas while Pt coordinates to the stable Ti-O surface terminations (see Fig. S4 for mechanism) [51,52]. Ideally, the SOMC synthesis protocol allows one to generate Pt single sites, but unavoidably small clusters were formed on $SrTiO_3$—especially after contact with water and under illumination (see Fig. S4 for description). Therefore, unless otherwise noted, all characterization steps here describe the samples after photocatalysis, which will be discussed later. The SOMC-derived grafted sample, namely, $Pt/SrTiO_3$ (GT), had a weight loading of 0.09 wt% as confirmed by ICP measurement. The $Pt/SrTiO_3$ (GT) treated at 300 °C in air was also obtained to exclusively increase the metal size with little impact on other parameters. The impregnation sample ($Pt/SrTiO_3$ (NP)) was obtained following the typical impregnation procedure with hexachloroplatinic acid. Our previous work demonstrated that 0.35 wt% Pt via wet impregnation was the optimal loading to maximize photocatalytic performance [29]. The optimized SOMC approach resulted in a sample with a maximum 0.09 wt% Pt loading, mainly regulated by the available surface hydroxyls on $SrTiO_3$. Herein, we compare our respectively optimized systems to study the overall catalytic effect of different size of Pt.

STEM images of $Pt/SrTiO_3$ (GT), $Pt/SrTiO_3$ (GT-300), and $Pt/SrTiO_3$ (NP) after photocatalytic OWS are shown in Fig. 3. The $Pt/SrTiO_3$ (GT) (Fig. 3a and Fig. S5) showed both single-atom Pt and Pt clusters ranging mostly below 2 nm (>0.85 fraction), which is consistent with the choice of small Pt cluster models used for the DFT calculations (Pt_1, Pt_{25}, and Pt_{50} in Fig. 1a). We note that the $SrTiO_3$ crystals are large and can reach widths of up to 500 nm; therefore, imaging single Pt atoms becomes challenging, and the single atoms could only be seen at the edges of the $SrTiO_3$ (see Fig. S5). The $Pt/SrTiO_3$ (GT-300) exhibited sintering, which shifted the size distribution to a larger maximum at ~2–3 nm in size (Fig. 3b). To this end, our Pt_{119} model for DFT is reasonably well-placed close to the 2 nm size distribution observed between the $Pt/SrTiO_3$ (GT) and (GT-300) samples in Fig. 1b. Finally, the $Pt/SrTiO_3$ (NP) consisted of a wide range of nanoparticle size ranging from 1 to 10 nm with the broad distribution centered at 3–4 nm (Fig. 3c). This is consistent with the non-uniform distribution nature typically obtained from the impregnation method.

3.3. Photocatalytic activity

The photocatalytic gas evolution time courses are detailed in Fig. 4. The samples tested were $Pt/SrTiO_3$ (GT), $Pt/SrTiO_3$ (GT-300), and $Pt/SrTiO_3$ (NP), and the reaction was conducted in 10 vol% methanol aqueous solution (Fig. 4a and a⇩), Milli-Q water (Fig. 4b and b⇩), or Milli-Q water in the presence of CO (Fig. 4c and c⇩) with UV light irradiation. The top part of the figure shows the quantity of the evolved gases, and the bottom part of the figure shows the rate of H_2 gas evolution (as representative data).

First, referring to H_2 evolution reaction from the methanol aqueous solution (Fig. 4a and a⇩), the photocatalytic performance was found to be in order: $Pt/SrTiO_3$ (NP) > $Pt/SrTiO_3$ (GT) > $Pt/SrTiO_3$ (GT-300). All samples show stable performance for at least 3 h. The half-reaction results in methanol indicate that the photocatalytic performance of the $Pt/SrTiO_3$ (GT) sample was higher than that of $Pt/SrTiO_3$ (GT-300) as a result of charge-separation capability and hydrogen evolution electrocatalytic

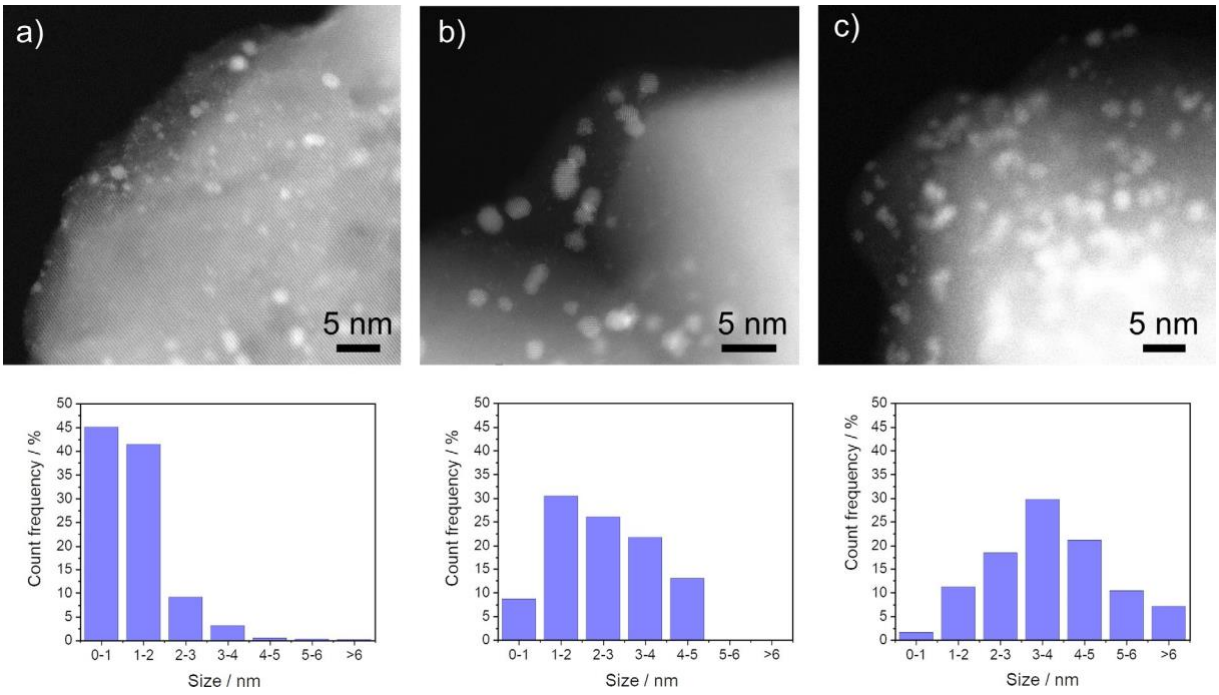

Fig. 3. STEM images of (a) Pt/$SrTiO_3$ (GT) prepared by the SOMC method, (b) Pt/$SrTiO_3$ (GT) treated at 300 °C (Pt/$SrTiO_3$ (GT-300)), and (c) Pt/$SrTiO_3$ (NP) prepared by impregnation method. The corresponding histograms of Pt particle sizes are underneath. Images were taken for the samples after photocatalysis.

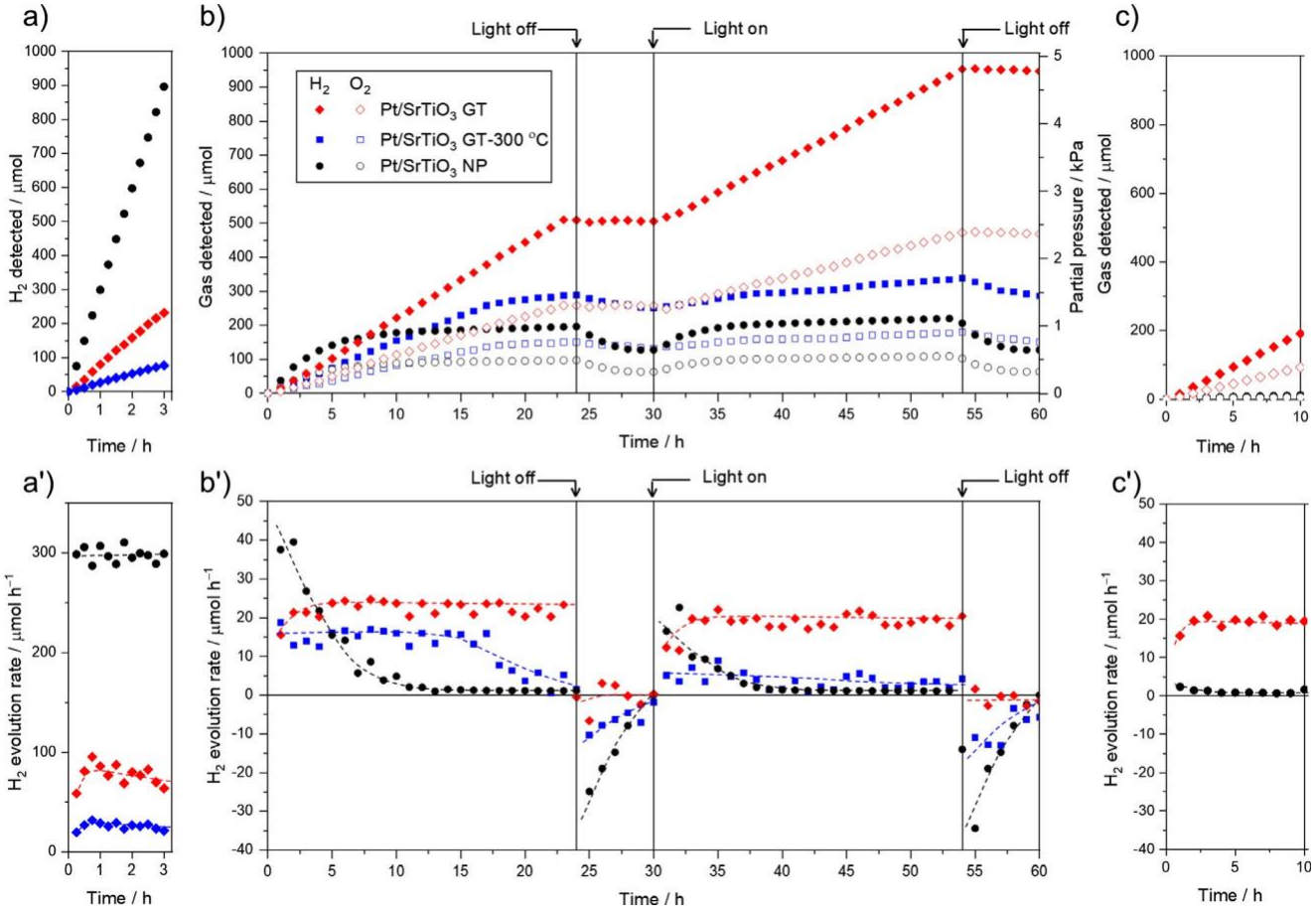

Fig. 4. Time on course (a, b, and c) of evolved gas quantity and gas evolution rate (a', b', and c') during photocatalytic reactions using Pt/$SrTiO_3$ (GT), Pt/$SrTiO_3$ (GT-300), and Pt/$SrTiO_3$ (NP) in (a,a') 10 vol% methanol aq. solution, (b,b') Milli-Q water, and (c,c') Milli-Q water with 0.6 kPa CO (100 mL of solution, 50 mg of photocatalyst, 490 mL of reactor volume).

capability. The 0.35 wt% Pt/$SrTiO_3$ (NP) tripled the H_2 evolution rate of the 0.09 wt% Pt/$SrTiO_3$ (GT) sample. Increasing the Pt loading on Pt/$SrTiO_3$ (GT) while maintaining atomic dispersion of Pt could lead to a more efficient photocatalyst; however, it is challenging due to the limited number of surface hydroxyls of the $SrTiO_3$ semiconductor for the SOMC synthesis.

Fig. 4(b and b') shows the result for OWS. The initial gas evolution rates were consistent with the order of the photocatalytic performance observed from methanol aqueous solutions when no products were present in the photoreactor, i.e., Pt/$SrTiO_3$ (NP) > Pt/$SrTiO_3$ (GT) > Pt/$SrTiO_3$ (GT-300). The Pt/$SrTiO_3$ (NP) achieved initial gas evolution rates of ~45 and ~22 μmol h^{-1} for H_2 and O_2, respectively, corresponding to an apparent quantum efficiency (AQE) of 17% at 350 nm. The stoichiometry of ~2:1 ratio for H_2:O_2 is consistent with the successful OWS. Nevertheless, the apparent gas evolution rates decreased drastically to almost zero after 5 h (Fig. 4b') when the products were accumulated to be ~1 kPa H_2 and ~0.5 kPa O_2. After 24 h of irradiation, the light source was turned off, and there was a decrease in H_2 and O_2 gases. The initial gas consumption rates were approximately ~35 and ~18 μmol h^{-1} for H_2 and O_2, respectively, which accounted for the almost equivalent with the forward OWS rate at the beginning of the reaction. From this result, the observed plateau after 10 h photocatalytic water splitting with Pt NPs is therefore not correlated with degradation of the photocatalyst and co-catalyst but rather ascribed to the steady-state equilibration between the forward water-splitting reaction and water-forming back reaction; thus, a strategy to suppress the back-reaction is essential for efficient OWS. Moreover, the main reason for the loss of OWS rates is the dark thermal back-reaction and not the oxygen reduction reaction (ORR) where excited electrons are competitively consumed instead of being used for H_2 evolution.

Fig. 4b and b' shows that Pt/$SrTiO_3$ (GT) had stable evolution rates from OWS of 23 and 12 μmol h^{-1} for H_2 and O_2, respectively, for the full 24 h irradiation period. The products' partial pressures could be accumulated far beyond those with Pt/$SrTiO_3$ (NP). The 2:1 H_2 to O_2 ratio in the products indicates successful OWS with an AQE of 8% at 350 nm. After the first 24 h of irradiation, the amount of accumulated H_2 and O_2 partial pressures remained unchanged in the photocatalytic reactor indicating a lack of water-forming catalytic activity on the Pt/$SrTiO_3$ (GT). Accordingly, resuming the illumination recovered the consistent photocatalytic rate of ~20 and ~10 μmol h^{-1} for H_2 and O_2, respectively. The difference in photocatalytic activity observed between the Pt/$SrTiO_3$ (NP) and Pt/$SrTiO_3$ (GT) is ascribed to the different thermal contributions of the water-forming reaction in the dark; this is a function of the size of the Pt catalyst on the surface. To further justify this conclusion, the Pt/$SrTiO_3$ (GT-300), i.e., Pt/$SrTiO_3$ (GT) heated at 300 °C led to larger Pt particles (Fig. 3) without altering other parameters. The sintered Pt catalyst had initial evolution rates of 15 and 8 μmol h^{-1} for H_2 and O_2, respectively, for the first 15 h. The lower photocatalytic rates of Pt/$SrTiO_3$ (GT-300) can be explained by the loss of Pt active sites from Pt/$SrTiO_3$ (GT). Although the Pt/$SrTiO_3$ (GT-300) accumulated ~1.4 kPa H_2 and ~0.7 kPa of O_2 up to ~15 h, the back reaction became obvious as observed by the decreasing rate of H_2 and O_2 evolutions similar to Pt/$SrTiO_3$ (NP). Considering the differences between Pt/$SrTiO_3$ (GT) and Pt/$SrTiO_3$ (GT-300), the Pt cluster size may be the main driving force leading to the water-formation back-reaction. This seems to have a threshold size of ~2 nm Pt clusters (Fig. 3). The finding is important because it is a rare case of a photocatalyst decorated with noble-metal co-catalysts that can be selective for the OWS forward-reaction without the use of a coating material.

Fig. 4(c and c') shows the result for OWS in the presence of CO gas. The 5% CO gas was first bubbled through the reactor solution for 30 min, and the photocatalytic reaction was performed with 5% CO gas atmosphere. The Pt/$SrTiO_3$ (NP) showed negligible OWS activity indicating that the Pt NPs were poisoned by the CO gas. The strong adsorption of CO gas to the surface Pt atoms of the NPs prevents the Pt from performing the hydrogen evolution reaction. The OWS requires the simultaneous production of H_2 and O_2 gas, and if one reaction is blocked, then the second reaction is consequently blocked. On the other hand, the Pt/$SrTiO_3$ (GT) could successfully complete the OWS reaction at a similar rate as in Fig. 4(a,a') OWS without the presence of CO with rates of ~19 and 8 μmol h^{-1} for H_2 and O_2, respectively. It is well known that CO gas poisons metallic Pt [55]; therefore, this finding is significant because it shows that if the Pt can maintain a higher oxidation state, then it can be insensitive to CO under catalytic conditions.

3.4. Characterization of the Pt state

A detailed characterization focusing on Pt/$SrTiO_3$ (GT) and Pt/$SrTiO_3$ (NP) follows. As described above, samples after photocatalytic reactions (labeled as ''spent" state) are chosen because the state of the samples is the most relevant to the photocatalytic performance. The grafted photocatalyst was also characterized before the photocatalytic test (labeled as ''pristine" state) to assess any changes in the Pt chemical environment due to irradiation under aqueous conditions.

X-ray absorption spectroscopy (XAS) operated at the Pt L_3-edge was collected, and the k^2-weighted EXAFS spectra and their related Fourier transforms (uncorrected from phase-shifts) are shown in Fig. S6 and Fig. 5a, respectively. The spectra of a metallic Pt powder and a platinum dioxide (PtO_2) powder are also provided as references. For the spent Pt/$SrTiO_3$ (NP) photocatalyst, the main contribution is noted between 1.6 and 3.2 Å, i.e., the spectra of the metallic Pt. The observed three-lobe peak is characteristic of the complex backscattering amplitude associated with a Pt-Pt scattering path (the Ramsauer-Townsend effect in EXAFS) [56]. Hence, the Pt/$SrTiO_3$ (NP) FT-EXAFS is consistent with the quantitative formation of metallic Pt nanoparticles on the surface of $SrTiO_3$. In contrast, the Fourier transform of the pristine Pt/$SrTiO_3$ (GT) shows only one prominent peak centered near ~1.5 Å, which is similar to the low R peak of the PtO_2 FT-EXAFS spectrum except that there is an additional shoulder on the right-hand side. The single prominent peak indicates the dominance of low Z backscatters in the first shell of platinum atoms. Those backscatters are most probably oxygen atoms from the $SrTiO_3$ support and/or long-distance coordinating water molecules because the Pt-C bonds from the original organometallic precursor must be hydrolyzed in the air. Furthermore, no significant bonding distance longer than 2.0 Å was detected: The platinum atoms in the pristine Pt/$SrTiO_3$ (GT) photocatalyst are either mononuclear species or form PtO_x clusters with such structural disorder that the Pt-Pt scattering cannot be observed.

After photocatalytic OWS, a restructuration of the grafted Pt atoms was obvious when considering the FT-EXAFS spectrum of spent Pt/$SrTiO_3$ (GT): (i) The main broad peak originally at ~1.5 Å is now clearly split in two contributions centered on 1.4 Å and 1.9 Å; (ii) Two new peaks have also appeared at 2.4 Å and 2.8 Å. To perform a relevant next nearest-neighbors identification of the newly observed features, a wavelet transformation analysis was applied to the EXAFS data (WT-EXAFS). The backscattering amplitude from neighboring atoms shows a significant k-dependence that determines the envelope of EXAFS oscillations v(k):[57] Lighter elements have their maximum backscattering amplitude at low wavenumbers while with increasing atomic number causes the maximum to shift towards higher k values.

The WT correlates with the backscattering amplitudes of individual paths in k-space and with their interatomic distances in R-space. Thus, it is a useful signal-processing tool for the

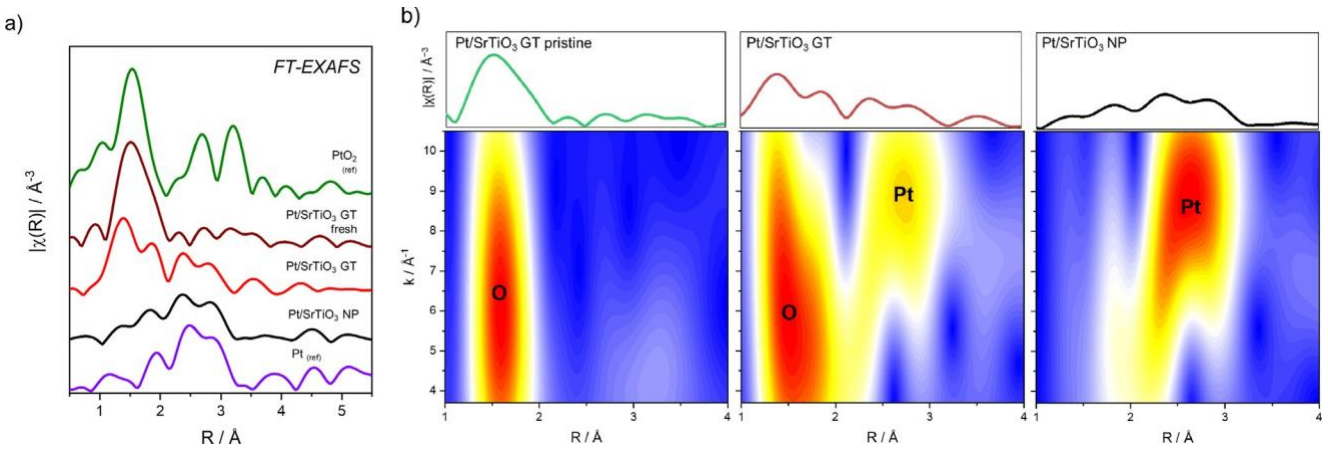

Fig. 5. (a) Magnitude of the Fourier transform (FT) of the k^2-weighed EXAFS measured at Pt L_3-edge of pristine Pt/$SrTiO_3$ (GT) before and after photocatalysis along with Pt/$SrTiO_3$ (NP) and two platinum references (metallic Pt and PtO_2 powders). (b) Contour plot of the wavelet transform (WT) magnitude showing the (k, R) localization of each FT-EXAFS contribution measured at the Pt L_3-edge for pristine and spent Pt/$SrTiO_3$ (GT) and Pt/$SrTiO_3$ (NP).

qualitative assignment of the backscatter identity. The wavelet-transform of the Fourier-filtered EXAFS is shown for pristine and spent Pt/$SrTiO_3$ (GT) together with the spent Pt/$SrTiO_3$ (NP) in Fig. 5b. The spent Pt/$SrTiO_3$ (GT) has two prominent maxima in the WT-EXAFS plot at the approximate coordinates (R = 1.5 Å, k = 6 $Å^{-1}$), (R = 2.6 Å, k = 8.5 $Å^{-1}$). Those two WT maxima are assigned to oxygen and a platinum backscatters by direct comparison with the FT-EXAFS of pristine Pt/$SrTiO_3$ (GT) and spent Pt/$SrTiO_3$ (NP), respectively, shown in Fig. 5a. This supports the STEM observations that a fraction of the isolated platinum atoms merged into clusters after the photocatalytic test. Note that the second peak in the first coordination shell is at 1.9 Å. While it is mainly assigned to an oxygen backscatter, it has also an overlapping contribution from the tail of the platinum backscatter. Attempts to perform quantitative EXAFS fitting failed to provide a reasonable residual possibly because of the heterogeneity of the samples.

The Pt L_3-edge HERFD-XANES spectra of the spent NP and GT samples along with the pristine GT sample and the reference Pt^0 and PtO_2 materials are presented in Fig. 6a. Lytle et al. showed that the intensity of the white line at the L_3 X-ray absorption edge is proportional to the d-electron vacancies; this is an indication of the oxidation state of the metal [58,59]. A higher oxidation state also shifts the absorption edge threshold to a higher energy (see Fig. S7 for a comparison between low and high resolution XANES). The HERFD-XANES white line intensity of the spent Pt/$SrTiO_3$ (NP) photocatalyst is comparable to the metallic powder reference (Fig. 6a). The position of the absorption edge threshold is also identical (11563.2 eV as calculated from the first derivative). This further points towards a metallic state of the Pt atoms. In addition, the high-energy resolved data of Pt/$SrTiO_3$ (NP) allows the detection of a shoulder located at 11567 eV just on the right-hand side of the white line. This feature was studied in detail before for the electrochemical oxidation of Pt nanoparticles thanks to the design of electrochemical cells fitted within an *operando* XANES-HERFD set-up [57,60].

Previous XAS works controlled the oxidation of Pt NPs supported on glassy carbon electrodes or Pt monolayers on the surface

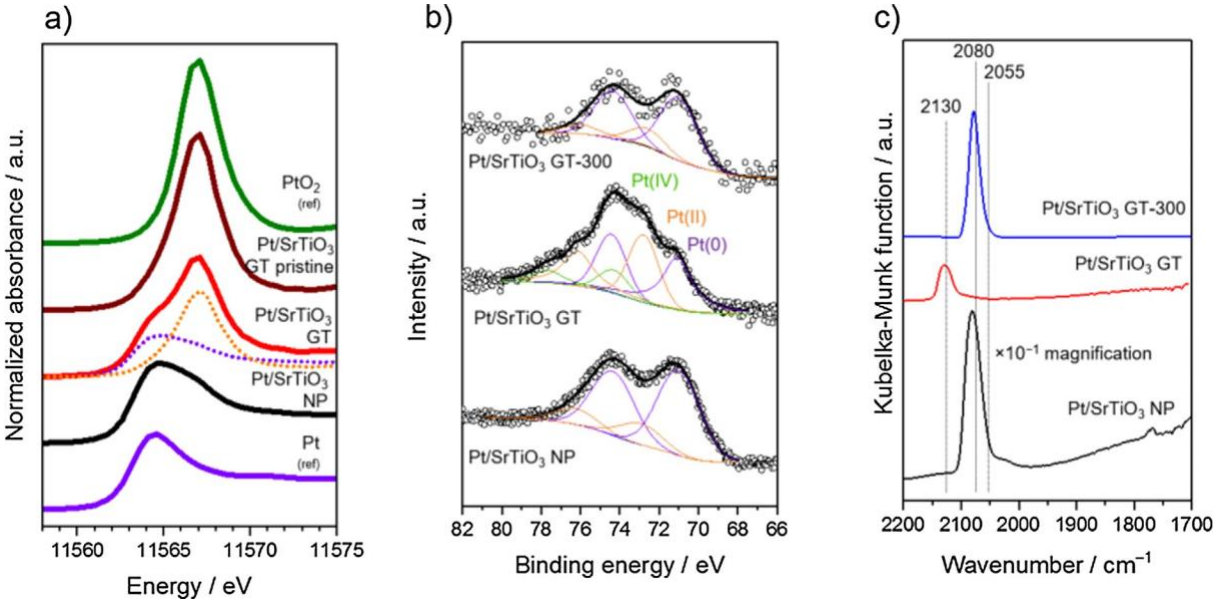

Fig. 6. (a) Pt-L3 edge HERFD–XANES of GT-Pt/$SrTiO_3$ before (pristine) and after photocatalysis, NP-Pt/$SrTiO_3$ after photocatalysis and two platinum references, e.g. metallic Pt and PtO_2 powders. The dotted lines are the respective the contribution determined from linear combination fitting using NP-Pt/$SrTiO_3$ after photocatalysis and GT-Pt/$SrTiO_3$ spectra before photocatalysis (pristine). (b) Pt 4f XPS of nanoparticle (NP) and grafted (GT) Pt/$SrTiO_3$ after photocatalysis. (c) CO DRIFTS of nanoparticle (NP), grafted (GT), and 300 °C-annealed grafted Pt (GT-300) obtained after the photocatalytic tests.

of a Rh monocrystal via the application of increasing anodic potentials at steady-state. Only subtle spectral changes were measured at potentials up to 1.0 V vs. RHE indicating low oxygen coverage on the Pt surface. At higher potentials, a high-energy contribution in the HERFD-XANES spectra significantly increases. This was interpreted by the quantitative formation of Pt oxide (similar to the shoulder at 11567 eV in Fig. 6a) [50]. We conclude that the Pt nanoparticles in the Pt/$SrTiO_3$ (NP) photocatalyst after the photocatalytic testing, although their most part is metallic, consists of a minor PtO_x species which is either on the surface of the nanoparticle or at the metal-support interface.

In contrast, the white line in the pristine Pt/$SrTiO_3$ (GT) HERFD-XANES spectrum is much higher and comparable to the PtO_2 reference (Fig. 6a). The absorption threshold also displays the same energy (11566.1 eV). In PtO_2, the platinum atoms are in the formal +IV oxidation state and are octahedrally coordinated with six oxygen atoms. Such resemblance with PtO_2 strongly suggests that the preparation of mononuclear platinum species immobilized on the surface of $SrTiO_3$ produces highly oxidized Pt(IV) atoms that are covalently grafted by oxygen bridges. After the photocatalytic test (GT-spent in Fig. 6a), the white line is separated in two well-defined peaks: One is similar to the original pristine photocatalyst (GT-pristine) and the other is similar to the metallic platinum observed in spent Pt/$SrTiO_3$ (NP). In order to retrieve quantitative information about the photocatalyst restructuration, a linear combination fitting was conducted using the spectra of the spent Pt/$SrTiO_3$ (NP) and pristine Pt/$SrTiO_3$ (GT) (R-factor = 0.1%). The results indicate that 51.4 ± 0.4% of the Pt atoms merge into metallic clusters while 48.6 ± 0.4% of the Pt atoms remain as an oxidized species. Fig. 6b shows the Pt 4f XPS spectra of the Pt/$SrTiO_3$ (NP) and Pt/$SrTiO_3$ (GT) after photocatalysis. This agrees with the findings in the XAS study. Furthermore, the HERFD-XANES spectroscopy results are therefore in-line with EXAFS and STEM imaging studies.

The CO DRIFTS data after photocatalysis is presented in Fig. 6c of the Pt/$SrTiO_3$ (NP), Pt/$SrTiO_3$ (GT), and the sintered Pt/$SrTiO_3$ (GT-300). Adsorbed CO on a Pt surface shifts the stretching vibration mode of gas-phase CO (frequency of ~2143 cm^{-1}) to lower wavenumbers due to the electron back-donation from the Pt atoms to the p*-orbitals of the CO molecules [17–19]. Previous studies have shown that the CO frequencies are closely related to the oxidation and coordination numbers of adsorbing Pt surface atoms as the strength of the CO–Pt bonding differs between corner, edge, and face sites [17–19,61]. The spent Pt/$SrTiO_3$ (NP) showed a large broad peak at ~2085 cm^{-1} corresponding to linearly bonded CO to ħ1 1 1ĩ Pt facet, and a shoulder peak at ~2050–2030 cm^{-1} corresponding to linear CO bonded to edge and corner sites of a NP [61]. The Pt/$SrTiO_3$ (GT) showed only one peak at 2130 cm^{-1} corresponding to CO binding to Pt^{2+} species [26,62,63]. Coordination of Pt^{2+} with CO has a higher wavenumber because there is less electron back-donation from the Pt orbitals to CO versus metallic Pt. This indicates that the exposed surface of the Pt species in the NP sample is primarily metallic and is primarily oxidized Pt^{2+} for the GT sample. The Pt/$SrTiO_3$ (GT-300) photocatalyst annealed at 300 °C showed one broad peak at ~2085 cm^{-1}, which is similar to the NP sample indicating more metallic behavior. The CO DRIFTS data was consistent with the XAS and XPS data and showed the existence of oxidized Pt species as a major component of the cluster.

4. Discussion

Our results show a distinctive change in catalytic behavior with Pt clusters that are below approximately ~2 nm in size. This allows it to selectively achieve the OWS reaction without a subsequent water-forming back reaction. On the contrary, larger Pt clusters show and maintain metallic character before and after illumination causing the back reaction. The DFT results show that the atoms in small Pt clusters (~100 atoms or less) are rich in electrons due to charge transfer from $SrTiO_3$ at thermal equilibration. The degree of EMSI at thermal equilibrium decreases both per Pt atom and per Pt particle with increasing cluster size. Looking into the literature [9,12–19], a threshold for changing the nature of Pt and the resulting reactivity consistently falls into the threshold of Pt sizes smaller than ~2 nm. The EMSI may indeed influence this exact value of the threshold depending on the electronic donation or withdrawal nature. The DFT calculations suggest that significant EMSI effects exist in Pt catalysts on $SrTiO_3$ when the number of atoms is fifty or below due to the intrinsic large work function of Pt and the confined and small number of atoms. As the cluster size decreases further, the DOS have a narrower d-band in the smallest supported cluster when the number of atoms reached a critical point (~25 atoms, <1 nm, Fig. 1c). At the same time, when the cluster size decreases below 2 nm, the coordination number changes accordingly (increase in edge and corner sites). It was previously reported that low-coordinated Pt has a much stronger binding energy to adsorbed species in spherical models [64–68]. Therefore, a significant increase in Pt-O binding is expected when the Pt cluster size is below 2 nm, even when Pt remains in a metallic state. Drastic changes in reactivity are expected when the small Pt clusters (<2 nm) exhibit a higher oxidation state as confirmed by XPS, XAS, and CO DRIFTS (even after photocatalytic reactions). Our results agree with Li et al. who showed that small oxidized Pt species have a positive Gibbs free energy for the adsorption of H_2 and O_2, which is consistent with the lack of H_2 consumption in the presence of O_2 [38]. Here, changing the nature of Pt from a metallic to an oxidized catalyst led to an intrinsic change in the reactivity and selectivity for the activation of the thermal water-formation back-reaction while keeping the site active for hydrogen evolution in photocatalytic OWS without the use of a core-shell material. The exact reaction mechanism remains unclear especially how the oxidized Pt clusters electrocatalytically evolve hydrogen. It is also well known that CO gas poisons metallic Pt [61]; however, our findings show that if the Pt can maintain a higher oxidation state, then it is insensitive to CO coordination and its site occupation for poisoning. In this context, Berto et al. reported that the CO-covered surface eliminated the back reaction for OWS [69]. It would be understandable that, when particle size distribution is broad and the photocatalyst contains both small and large Pt particles, CO poisons the large metallic particles that cause back reaction. Thus, the photocatalyst with smaller oxidized particles remain active for selective OWS. Such poison-free function of the oxidized metal catalyst has great potential for the reaction under severe reaction conditions where impurities such as CO are present. Overall, the arguments regarding the ultrafine (~2 nm) PtO_x clusters discussed above may be applicable to many other metals in selective electrocatalysis and photocatalysis.

5. Conclusions

Our study shows that ultrafine (~100 Pt atoms or <~2 nm) PtO_x clusters supported on $SrTiO_3$ enables successful photocatalytic OWS without introducing thermal H_2 and O_2 recombination to H_2O. The Pt/$SrTiO_3$ (GT) photocatalyst consisting of ultrafine PtO_x clusters was stable for a 48-h OWS reaction with an AQE of 8% (k = 350 nm). Sintering the clusters to larger particles promoted a thermal water-forming back reaction. Although the Pt/$SrTiO_3$ (NP) had an initial AQE of 17% for the first hour (k = 350 nm), the net rate dropped to zero after 5 h due to the competing water formation back reaction. Thus, such nanoparticles supported on the semiconductor cannot effectively drive photocatalytic OWS at steady-state conditions. The TEM, CO DRIFTS, XAS, and XPS characterizations indicate a mixture of Pt single atoms and small clusters

in Pt/$SrTiO_3$ (GT), which exhibited a higher oxidation state even after the photocatalytic test. In contrast, the larger Pt clusters in Pt/$SrTiO_3$ (NP) after illumination were completely reduced to Pt^0. The ease of oxidation of small clusters was supported by DFT calculation, which showed an EMSI size-effect when the number of Pt atoms are approximately 100 or less (<2 nm). Overall, Pt clusters <~2 nm supported on $SrTiO_3$ preferred to exist in its oxidized form, which led to a distinctive difference in catalytic behavior compared with the larger (>~2 nm) Pt nanoparticles who preferred to exist in its metallic state. Future studies should increase the loading and control the spatial distribution, dispersion, and uniformity of Pt sites on the support materials for further optimization of the photocatalytic performance.

Acknowledgements

The research reported in this work was supported by the King Abdullah University of Science and Technology. The FAME-UHD project is financially supported by the French large loan EquipEx (EcoX, ANR-10-EQPX-27-01), the CEA-CNRS CRG consortium and the INSU CNRS Institute. The authors thank the SYSPROD project and AXELERA Pôle de Compétitivité for financial support (PSMN Data Center). They thank also IDRIS in Paris, CINES in Montpellier, TGCC in Grenoble (project 609, GENCI/CT8) and PSMN in Lyon for CPU time and assistance.

Appendix A. Supplementary material

Supplementary data to this article can be found online at https://doi.org/10.1016/j.jcat.2019.06.045.

References

[1] L. Liu, A. Corma, Metal catalysts for heterogeneous catalysis: from single atoms to nanoclusters and nanoparticles, Chem. Rev. 118 (2018) 4981–5079.
[2] S. Vajda, M.G. White, Catalysis applications of size-selected cluster deposition, ACS Catal. 5 (2015) 7152–7176.
[3] T. Houwaart, T. Le Bahers, P. Sautet, W. Auwärter, K. Seufert, J.V. Barth, M. Bocquet, Scrutinizing individual CoTPP molecule adsorbed on coinage metal surfaces from the interplay of STM experiment and theory, Surf. Sci. 635 (2015) 108–114.
[4] S. Zhang, Y. Lu, Y. Zhang, C. Peng, H. Liu, Halogen-bond-based molecular self-assembly on graphene surface: a first-principles study, J. Phys. Chem. C 4451–4461 (2017).
[5] W. Zhu, R. Michalsky, Ö. Metin, H. Lv, S. Guo, C. Wright, X. Sun, A. Peterson, S. Sun, Monodisperse Au nanoparticles for selective electrocatalytic reduction of CO_2 to CO, J. Am. Chem. Soc. 135 (2013) 16833–16836.
[6] G.A. Somorjal, J. Carrazza, Structure sensitivity of catalytic reactions, Ind. Eng. Chem. Fundam. 25 (1986) 63–69.
[7] M. Che, C.O. Bennett, The influence of particle size on the catalytic properties of supported metals, Adv. Catal. 36 (1989) 55–172.
[8] S.J. Tauster, Strong metal-support interactions, Acc. Chem. Res. 20 (1987) 389–394.
[9] Y. Lykhach, S.M. Kozlov, T. Skála, A. Tovt, V. Stetsovych, N. Tsud, F. Dvořák, V. Johánek, A. Neitzel, J. Mysliveček, S. Fabris, V. Matolín, K.M. Neyman, J. Libuda, Counting electrons on supported nanoparticles, Nat. Mater. 15 (2015) 284–288.
[10] S.M. Kozlov, K.M. Neyman, Effects of electron transfer in model catalysts composed of Pt nanoparticles on CeO_2(111) surface, J. Catal. 344 (2016) 507–514.
[11] N.M. Markovic, T.J. Schmidt, V. Stamenkovic, P.N. Ross, Oxygen reduction reaction on Pt and Pt bimetallic surfaces: a selective review, Fuel Cells. 1 (2001) 105–116.
[12] K. Kinoshita, Particle size effects for oxygen reduction on highly dispersed platinum in acid electrolytes, J. Electrochem. Soc. 137 (1990) 845.
[13] M. Peuckert, T. Yoneda, R.A.D. Betta, M. Boudart, Oxygen reduction on small supported platinum particles, J. Electrochem. Soc. 133 (1986) 944–947.
[14] K. Wettergren, A. Hellman, F. Cavalca, V.P. Zhdanov, C. Langhammer, Unravelling the dependence of hydrogen oxidation kinetics on the size of pt nanoparticles by in operando nanoplasmonic temperature sensing, Nano Lett. 15 (2015) 574–580.
[15] Y. Sun, Y. Dai, Y. Liu, S. Chen, A rotating disk electrode study of the particle size effects of Pt for the hydrogen oxidation reaction, PCCP 14 (2012) 2278–2285.
[16] F. Calle-Vallejo, J. Tymoczko, V. Colic, Q. Huy Vu, M.D. Pohl, K. Morgenstern, D. Loffreda, P. Sautet, W. Schuhmann, A.S. Bandarenka, Science 350 (2015) 185–189.
[17] G. Blyholder, Molecular orbitals views of chemisorbed carbon monoxide, J. Phys. Chem. 68 (1964) 2772–2777.
[18] M. Primet, J.M. Basset, M.V. Mathieu, M. Prettre, Infrared study of CO adsorbed on Pt/Al_2O_3. A method for dtermining metal-adsorbate interactions, J. Catal. 29 (1973) 213–223.
[19] H. Wang, Y. Wang, Z. Zhu, A. Sapi, K. An, G. Kennedy, W.D. Michalak, G.A. Somorjai, Influence of size-induced oxidation state of platinum nanoparticles on selectivity and activity in catalytic methanol oxidation in the Gas phase, Nano Lett. 13 (2013) 2976–2979.
[20] L. Bai, S. Zhang, Q. Chen, C. Gao, Synthesis of ultrasmall platinum nanoparticles on polymer nanoshells for size-dependent catalytic oxidation reactions, ACS Appl. Mater. Interfaces 9 (2017) 9710–9717.
[21] J. Kim, H.-E. Kim, H. Lee, Single-atom catalysts of precious metals for electrochemical reactions, ChemSusChem 11 (2018) 104–113.
[22] X.-F. Yang, A. Wang, B. Qiao, J. Li, J. Liu, T. Zhang, Single-atom catalysts: a new frontier in heterogeneous catalysis, Acc. Chem. Res. 46 (2013) 1740–1748.
[23] A. Wang, J. Li, T. Zhang, Heterogeneous single-atom catalysis, Nat. Rev. Chem. 2 (2018) 65–81.
[24] J. Liu, Catalysis by supported single metal atoms, ACS Catal. 7 (2017) 34–59.
[25] M. Yang, J. Liu, S. Lee, B. Zugic, J. Huang, L.F. Allard, M. Flytzani-stephanopoulos, A common single-site Pt(II)−O(OH)$_x$ species stabilized by sodium on ‘‘Active” and ‘‘Inert” supports catalyzes the water-gas shift reaction, J. Am. Chem. Soc. 137 (2015) 3470–3473.
[26] K. Ding, A. Gulec, A.M. Johnson, N.M. Schweitzer, G.D. Stucky, L.D. Marks, P.C. Stair, Identification of active sites in CO oxidation and water-gas shift over supported Pt catalysts, Science 350 (2015) 189–192.
[27] K. Maeda, K. Teramura, D. Lu, N. Saito, Y. Inoue, K. Domen, Noble-metal/Cr_2O_3 core/shell nanoparticles as a cocatalyst for photocatalytic overall water splitting, Angew. Chem. Int. Ed. 45 (2006) 7806–7809.
[28] M. Yoshida, K. Takanabe, K. Maeda, A. Ishikawa, J. Kubota, Y. Sakata, Y. Ikezawa, K. Domen, Role and function of noble-metal/Cr-layer core/shell structure cocatalysts for photocatalytic overall water splitting studied by model electrodes, J. Phys. Chem. C 113 (2009) 10151–10157.
[29] M. Qureshi, T. Shinagawa, N. Tsiapis, K. Takanabe, Exclusive hydrogen generation by electrocatalysts coated with an amorphous chromium-based layer achieving efficient overall water splitting, ACS Sustain. Chem. Eng. 5 (2017) 8079–8088.
[30] K. Domen, A. Kudo, T. Onishi, N. Kosugi, H. Kuroda, Photocatalytic decomposition of water into H_2 and O_2 over NiO-$SrTiO_3$ powder. 1. Structure, J. Phys. Chem. 90 (1986) 292–295.
[31] K. Han, T. Kreuger, B. Mei, G. Mul, Transient behavior of Ni@NiO_x functionalized $SrTiO_3$ in overall water splitting, ACS Catal. 7 (2017) 1610–1614.
[32] L. Zhang, Q. Liu, T. Aoki, P.A. Crozier, Structural evolution during photocorrosion of Ni/NiO Core/shell cocatalyst on TiO_2, J. Phys. Chem. C 119 (2015) 7207–7214.
[33] A.T. Garcia-Esparza, T. Shinagawa, S. Ould-Chikh, M. Qureshi, X. Peng, N. Wei, D.H. Anjum, A. Clo, T.C. Weng, D. Nordlund, D. Sokaras, J. Kubota, K. Domen, K. Takanabe, An oxygen-insensitive hydrogen evolution catalyst coated by a molybdenum-based layer for overall water splitting, Angew. Chemie Int. Ed. 56 (2017) 5780–5784.
[34] N.Y. Labrador, X. Li, Y. Liu, J.T. Koberstein, R. Wang, H. Tan, T.P. Moffat, D.V. Esposito, Enhanced performance of Si MIS photocathodes containing oxide-coated nanoparticle electrocatalysts, Nano Lett. 16 (2016) 6452–6459.
[35] J.A. Bau, K. Takanabe, Ultrathin microporous SiO_2 membranes photodeposited on hydrogen evolving catalysts enabling overall water splitting, ACS Catal. 7 (2017) 7931–7940.
[36] M. Yoshida, K. Maeda, D. Lu, J. Kubota, K. Domen, Lanthanoid oxide layers on rhodium-loaded ($Ga_{1-x}Zn_x$)($N_{1-x}O_x$) photocatalyst as a modifier for overall water splitting under visible-light irradiation, J. Phys. Chem. C 117 (2013) 14000–14006.
[37] T. Takata, C. Pan, M. Nakabayashi, N. Shibata, K. Domen, Fabrication of a core-shell-type photocatalyst via photodeposition of group IV and V transition metal oxyhydroxides: an effective surface modification method for overall water splitting, J. Am. Chem. Soc. 137 (2015) 9627–9634.
[38] Y.H. Li, J. Xing, Z.J. Chen, Z. Li, F. Tian, L.R. Zheng, H.F. Wang, P. Hu, H.J. Zhao, H. G. Yang, Unidirectional suppression of hydrogen oxidation on oxidized platinum clusters, Nat. Commun. 4 (2013) 1–7.
[39] Y. Ham, T. Hisatomi, Y. Goto, Y. Moriya, Y. Sakata, A. Yamakata, J. Kubota, K. Domen, Flux-mediated doping of $SrTiO_3$ photocatalysts for efficient overall water splitting, J. Mater. Chem. A 4 (2016) 3027–3033.
[40] B. Ravel, M. Newville, ATHENA, ARTEMIS, HEPHAESTUS: data analysis for X-ray absorption spectroscopy using IFEFFIT, J. Synchrotron Radiat. 12 (2005) 537–541.
[41] M. Munoz, P. Argoul, F. Farges, Continuous cauchy wavelet transform analyses of EXAFS spectra: a qualitative approach, Am. Mineral. 88 (2003) 694–700.
[42] G. Kresse, D. Joubert, From ultrasoft pseudopotentials to the projector augmented-wave method, Phys. Rev. B – Condens. Matter Mater. Phys. 59 (1999) 1758–1775.
[43] S.N. Steinmann, P. Sautet, C. Michel, Solvation free energies for periodic surfaces: comparison of implicit and explicit solvation models, PCCP 18 (2016) 31850–31861.
[44] S.N. Steinmann, C. Michel, R. Schwiedernoch, J.S. Filhol, P. Sautet, Modeling the HCOOH/CO_2 electrocatalytic reaction: when details are key, ChemPhysChem 16 (2015) 2307–2311.
[45] S.N. Steinmann, C. Michel, R. Schwiedernoch, P. Sautet, Impacts of electrode potentials and solvents on the electroreduction of CO_2: a comparison of theoretical approaches, PCCP 17 (2015) 13949–13963.

[46] S.N. Steinmann, C. Corminboeuf, Comprehensive benchmarking of a density-dependent dispersion correction, J. Chem. Theory Comput. 7 (2011) 3567–3577.
[47] J.M.P. Martirez, S. Kim, E.H. Morales, B.T. Diroll, M. Cargnello, T.R. Gordon, C.B. Murray, D.A. Bonnell, A.M. Rappe, Synergistic oxygen evolving activity of a TiO_2-rich reconstructed $SrTiO_3$(001) surface, J. Am. Chem. Soc. 137 (2015) 2939–2947.
[48] F. Calle-Vallejo, R.F. de Morais, F. Illas, D. Loffreda, P. Sautet, Affordable estimation of solvation contributions to the adsorption energies of oxygenates on metal nanoparticles, J. Phys. Chem. C 123 (2019) 5578–5582.
[49] E. Heifets, R.I. Eglitis, E.A. Kotomin, J. Maier, G. Borstel, Ab initio modeling of surface structure for $SrTiO_3$ perovskite crystals, Phys. Rev. B. 64 (2001) 235417.
[50] J. Padilla, D. Vanderbilt, Ab initio study of $SrTiO_3$ surfaces, Surf. Sci. 418 (1998) 64–70.
[51] G. Jeantelot, S. Ould-Chikh, J. Sofack-Kreutzer, E. Abou-Hamad, D.H. Anjum, S. Lopatin, M. Harb, L. Cavallo, J.-M. Basset, Morphology control of anatase TiO2 for well-defined surface chemistry, PCCP 20 (2018) 14362–14373.
[52] J.-M. Basset, F. Lefebvre, C. Santini, Surface organometallic chemistry: some fundamental features including the coordination effects of the support, Coord. Chem. Rev. 178–180 (1998) 1703–1723.
[53] C. Dessal, A. Sangnier, C. Chizallet, C. Dujardin, F. Morfin, J.-L. Rousset, M. Aouine, M. Bugnet, P. Afanasiev, L. Piccolo, Atmosphere-dependent stability and mobility of catalytic Pt single atoms and clusters on c-Al_2O_3, Nanoscale. 11 (2019) 6897–6904.
[54] A. Sangnier, M. Matrat, A. Nicolle, C. Dujardin, C. Chizallet, Multiscale approach to the dissociative adsorption of oxygen on a highly dispersed platinum supported on c-Al_2O_3, J. Phys. Chem. C 122 (2018) 26974–26986.
[55] C.H. Bartholomew, Mechanisms of catalyst deactivation, Appl. Catal. A Gen. 212 (2001) 17–60.
[56] A.G. McKale, B.W. Veal, A.P. Paulikas, S.K. Chan, G.S. Knapp, Generalized Ramsauer-Townsend effect in extended x-ray-absorption fine structure, Phys. Rev. B. 38 (1988) 10919–10921.
[57] D. Friebel, D.J. Miller, C.P. O'Grady, T. Anniyev, J. Bargar, U. Bergmann, H. Ogasawara, K.T. Wikfeldt, L.G.M. Pettersson, A. Nilsson, In situ X-ray probing reveals fingerprints of surface platinum oxide, PCCP 13 (2011) 262–266.
[58] F.W. Lytle, Determination of d-band occupancy in pure metals and supported catalysts by measurement of the LIII X-ray absorption threshold, J. Catal. 43 (1976) 376–379.
[59] F.W. Lytle, P.S.P. Wei, R.B. Greegor, G.H. Via, J.H. Sinfelt, Effect of chemical environment on magnitude of x-ray absorption resonance at LIIIedges. Studies on metallic elements, compounds, and catalysts, J. Chem. Phys. 70 (1979) 4849–4855.
[60] L.R. Merte, F. Behafarid, D.J. Miller, D. Friebel, S. Cho, F. Mbuga, D. Sokaras, R. Alonso-Mori, T.C. Weng, D. Nordlund, A. Nilsson, B. Roldan Cuenya, Electrochemical oxidation of size-selected pt nanoparticles studied using in situ high-energy-resolution X-ray absorption spectroscopy, ACS Catal. 2 (2012) 2371–2376.
[61] S.K. Cheah, V.P. Bernardet, A.A. Franco, O. Lemaire, P. Gelin, Study of CO and hydrogen interactions on carbon-supported pt nanoparticles by quadrupole mass spectrometry and operando diffuse reflectance FTIR spectroscopy, J. Phys. Chem. C 117 (2013) 22756–22767.
[62] K.I. Hadjiivanov, IR study of CO and H_2O coadsorption on Pt^{n+}/TiO_2 and Pt/TiO_2 samples, J. Chem. Soc., Faraday Trans. 94 (1998) 1901–1904.
[63] K. Balakrishnan, A. Sachdev, J. Schwank, Chemisorption and FTIR study of bimetallic Pt-Au/SiO_2 catalysts, J. Catal. 121 (1990) 441–455.
[64] B.C. Han, C.R. Miranda, G. Ceder, Effect of particle size and surface structure on adsorption of O and OH on platinum nanoparticles: a first-principles study, Phys. Rev. B. 77 (2008) 075410.
[65] M. Shao, A. Peles, K. Shoemaker, Electrocatalysis on platinum nanoparticles: particle size effect on oxygen reduction reaction activity, Nano Lett. 11 (2011) 3714–3719.
[66] X. Lin, N.J. Ramer, A.M. Rappe, K.C. Hass, W.F. Schneider, B.L. Trout, Effect of particle size on the adsorption of O and S atoms on Pt: a density-functional theory study, J. Phys. Chem. B 105 (2001) 7739–7747.
[67] Y. Xu, W.A. Shelton, W.F. Schneider, Effect of particle size on the oxidizability of platinum clusters, J. Phys. Chem. A 110 (2006) 5839–5846.
[68] G.A. Tritsaris, J. Greeley, J. Rossmeisl, J.K. Nørskov, Atomic-scale modeling of particle size effects for the oxygen reduction reaction on Pt, Catal. Lett. 141 (2011) 909–913.
[69] T.F. Berto, K.E. Sanwald, J.P. Byers, N.D. Browning, O.Y. Gutiérrez, J.A. Lercher, Enabling overall water splitting on photocatalysts by CO-covered noble metal co-catalysts, J. Phys. Chem. Lett. 7 (2016) 4358–4362.